Supporting Information

A facile precursor route towards the synthesis of $Fe_{1-x}S$@NC-rGO composite anode materials for high-performance lithium-ion batteries

Guanghao Zhan[a,b], Ruibo Yan[b,c], Wenhua Liao[b,c], Qianqian Hu*[b], Xiaoying Huang*[b]

[a.]College of Chemistry, Fuzhou University, Fuzhou, Fujian 350108, PR. China

[b] State Key Laboratory of Structural Chemistry, Fujian Institute of Research on the Structure of Matter, Chinese Academy of Sciences, Fuzhou 350002, PR China

[c] College of Chemistry and Materials Science, Fujian Normal University, Fuzhou, Fujian 350007, PR China

*Corresponding author
E-mail: xyhuang@fjirsm.ac.cn (HuangXY); huqianqian@fjirsm.ac.cn (HuQQ)

1. Experimental

1.1. Preparation of Organic-Inorganic Composite

$Fe_{1-x}S(en)_{0.5}$ nanowires were prepared by a facile solvothermal process. Typically, 1.5 mmol of $FeCl_2 \cdot 4H_2O$ and 3 mmol of thioacetamide were mixed in a Teflon-lined stainless-steel autoclave with the capacity of 28 mL, and then 10 mL of ethylenediamine was added. After fully stirred, the autoclave was kept at 180 °C for 4 days. The brown needle flocs obtained from the autoclave were filtered and washed in methanol for three times, and the resulting product was dried in the vacuum at 70 °C for 12 h.

1.2. Preparation of $Fe_{1-x}S$@NC-rGO Composites

45 mg of $Fe_{1-x}S(en)_{0.5}$ was encapsulated in a quartz tube (1 cm in diameter and 15 cm in length), which was then evacuated and sealed. The tube was heated to 700 °C with a heating rate of 2 °C min^{-1} in a muffle furnace and then held for 2 h. Before taking out of the product, the furnace was naturally drop to room temperature. Then, the black N-doped carbon-coated $Fe_{1-x}S$ sheets ($Fe_{1-x}S$@NC) were obtained.

$Fe_{1-x}S$@NC-rGO composites were prepared by a simple stirring at room temperature and subsequent heat treatment. In the typical synthesis, 66.9 mg of $Fe_{1-x}S$@NC was added to 50 mL of rGO[1] ethanol solution with different concentration (0.0, 0.5, 1.0, 2.0 mg mL^{-1}), and then continuously stirred for 1 h to form the assembly composites. The obtained suspension was centrifuged at 8000 rpm, and then the bottom sample was collected and dried in a vacuum oven at 60 °C for 12 h. The dried product was annealed at 350 °C for 2 h in the tube furnace under the mixed atmosphere of H_2 and N_2 (10% H_2 in volume). The resulting composites obtained using the rGO solutions with concentrations of 0.0, 0.5, 1.0, 2.0 mg mL^{-1}, are denoted as $Fe_{1-x}S$@NC, $Fe_{1-x}S$@NC-rGO-1, $Fe_{1-x}S$@NC-rGO-2, and $Fe_{1-x}S$@NC-rGO-3, respectively.

1.3. Materials characterizations

The reagents used are commercially available products without further purification. The phase composition and content of the composites were analyzed using an X-ray powder diffractometer (PXRD Rigaku Xray Miniflex ii, Cu Kα radiation source,

λ=1.5418 Å) and an elemental analyzer (EA ELEMENTAR VARIO EL CUBE). The structural characteristics of the composites were measured by field emission scanning electron microscopy (FESEM SU8010) and transmission electron microscopy (TEM FEI Talos F200S). Raman spectra are analyzed on a Horiba Labram HR800 Evolution Raman spectrometer. Thermogravimetric spectra were obtained on a thermal analyzer (TGA NETZSCH STA449F3). The specific surface area (BET) was calculated by automatic static chemical adsorption instrument (ASAP 2020). X-ray photoelectron spectroscopy was measured on an X-ray photoelectron spectrometer (XPS ESCALAB 250Xi Al Kα λ=8 Å, *hv*=1486.6 eV).

1.4. Electrochemical measurements

The composite material was assembled into a CR 2032 button battery for electrochemical performance testing. 70 wt% of active material, 20 wt% of conductive carbon black, 10 wt% of polyvinylidene fluoride (PVDF), and an appropriate amount of 1-N-methyl-2-pyrrolidone (NMP) were mixed, and the slurry was evenly coated on the copper foil as a working electrode. It is dried in a blast furnace at 80 °C for 6 h and then placed in a vacuum oven at 120 °C for 12 h. The dried copper foil was pressed into a 1.2 cm wafer on a 10 MPa tableting machine, and the mass of active material was about 1.0 mg cm^{-2}. The storage performance of lithium was studied with the prepared materials. Lithium foil acted as reference electrode and Celgard 2325 acted as separator. The electrolyte is composed of 1.0 M $LiPF_6$ dissolved in ethylene carbonate/dimethyl carbonate/diethyl carbonate (volume ratio of 1 : 1 : 1) (containing 5 vol% vinyl fluoride carbonate). Electrochemical impedance spectroscopy (EIS) and cyclic voltammetry (CV) were performed on an electrochemical workstation (CHI660E). Constant current discharge/charge cycles and rate performance tests are performed on LAND 2001A software.

Table. S1. Elemental analysis (EA) results of $Fe_{1-x}S$@NC and $Fe_{1-x}S$@NC-rGO.

mateiral	N (wt %)	C (wt %)
$Fe_{1-x}S$@NC	4.4	17.92
$Fe_{1-x}S$@NC-rGO-1	3.72	21.6
$Fe_{1-x}S$@NC-rGO-2	3.65	25.44
$Fe_{1-x}S$@NC-rGO-3	0.67	31.38

Table. S2. Comparison of high current cycling performance for $Fe_{1-x}S$@NC-rGO-2 composite and previously reported iron sulfide-based materials.

material	current density (mA g^{-1})	number of cycles	Capacity (mhA g^{-1})	reference
FeS/PC	0.1	65	592	[2]
FeS_2@N/S-C	1.0	1000	528	[3]
FeS@graphene	0.1	100	838	[4]
Fe_7S_8/C	1.0	100	689.4	[5]
FeS@NSC	1.0	240	611	[6]
FeS@PWS900	5.0	500	1057	[7]
3D GCs/FeS	0.5	160	848	[8]
FeS/N-doped-C	1.0	200	621	[9]
FeS@N-C	1.0	500	1061	[10]
$Fe_{1-x}S$@C	1.0	100	952	[11]
FeS/Fe_3C	0.1	200	712.2	[12]
FeS@rGO	5.0	1000	325	[13]
FeS_2@rGO	5.0	700	340	[14]
FeS_2@C	2.0	1000	637	[15]
FeS@CNS	1.0	150	701	[16]
FeS@C-N	0.1	100	983	[17]
G@FeS-GNRs	0.4	100	536	[18]
FeS@NS-CR	1.0	500	500	[19]
MOF-Derived FeS/C	0.1	500	830	[20]
FeS/Fe_3C	1.0	800	610	[12]
FeS@CMK-5	5.0	1500	1000	[21]
$Fe_{1-x}S$@C NW	0.2	120	583	[22]
$Fe_{1-x}S$@C/MCMB	0.2	120	531.7	[23]
FS/N-HCUF-700S	0.1	200	632.1	[24]
$Fe_{1-x}S$@NC	5.0	150	666	[25]
$Fe_{1-x}S$@rGO	0.1	200	632.1	[26]
Our work	1.0	1690	939.5	

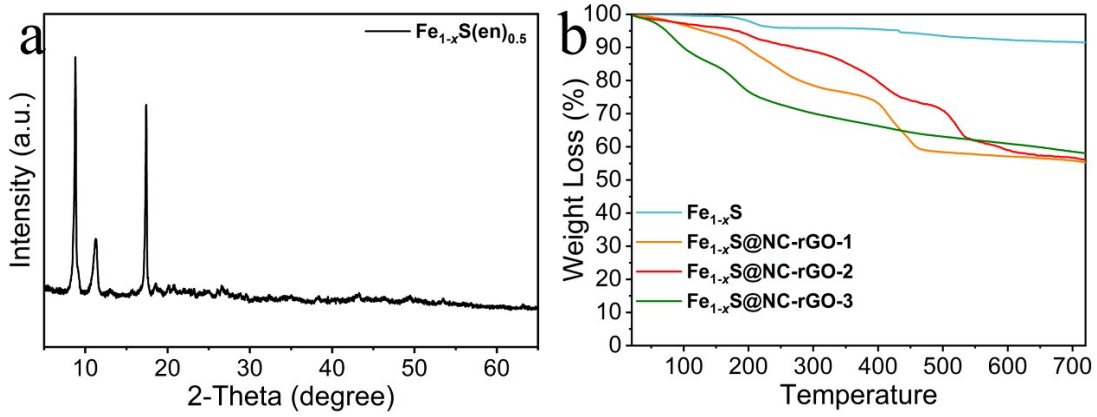

Fig. S1. (a) XRD patterns of $Fe_{1-x}S(en)_{0.5}$. (b) The thermogravimetric curves of $Fe_{1-x}S$@NC and $Fe_{1-x}S$@NC-rGO.

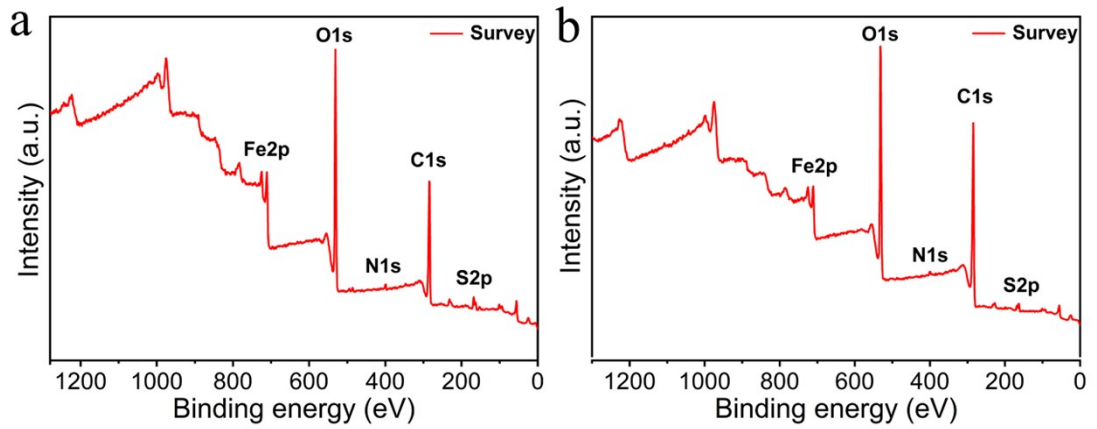

Fig. S2. Survey XPS spectra of (a) $Fe_{1-x}S$@NC-1 and (b) $Fe_{1-x}S$@NC-3.

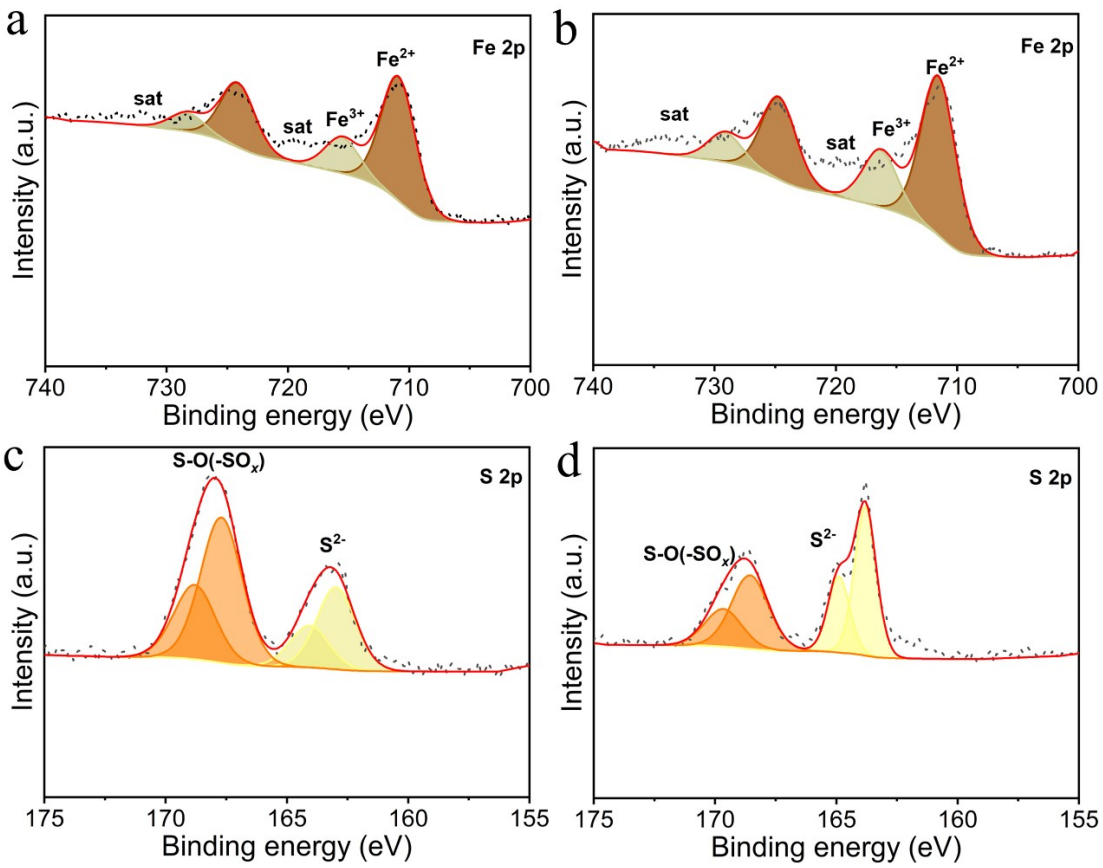

Fig. S3. Fe 2p XPS spectra of (a) $Fe_{1-x}S$@NC-1 and (b) $Fe_{1-x}S$@NC-3; (c) S 2p XPS spectra of (d) $Fe_{1-x}S$@NC-1 and $Fe_{1-x}S$@NC-3.

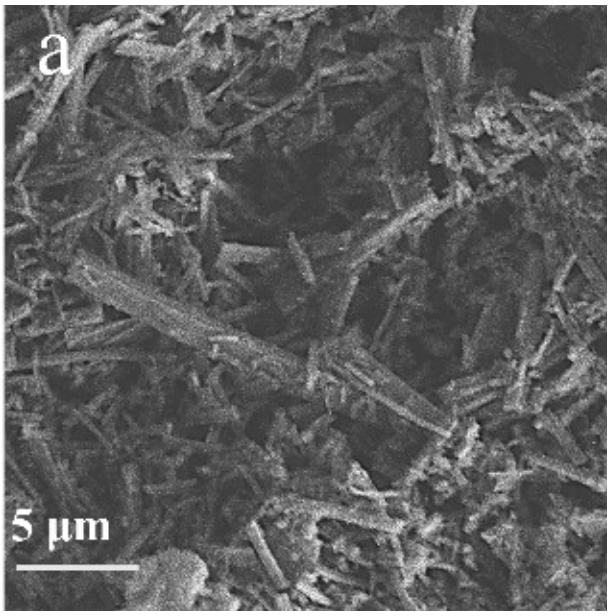

Fig. S4. (a) SEM image of $Fe_{1-x}S(en)_{0.5}$.

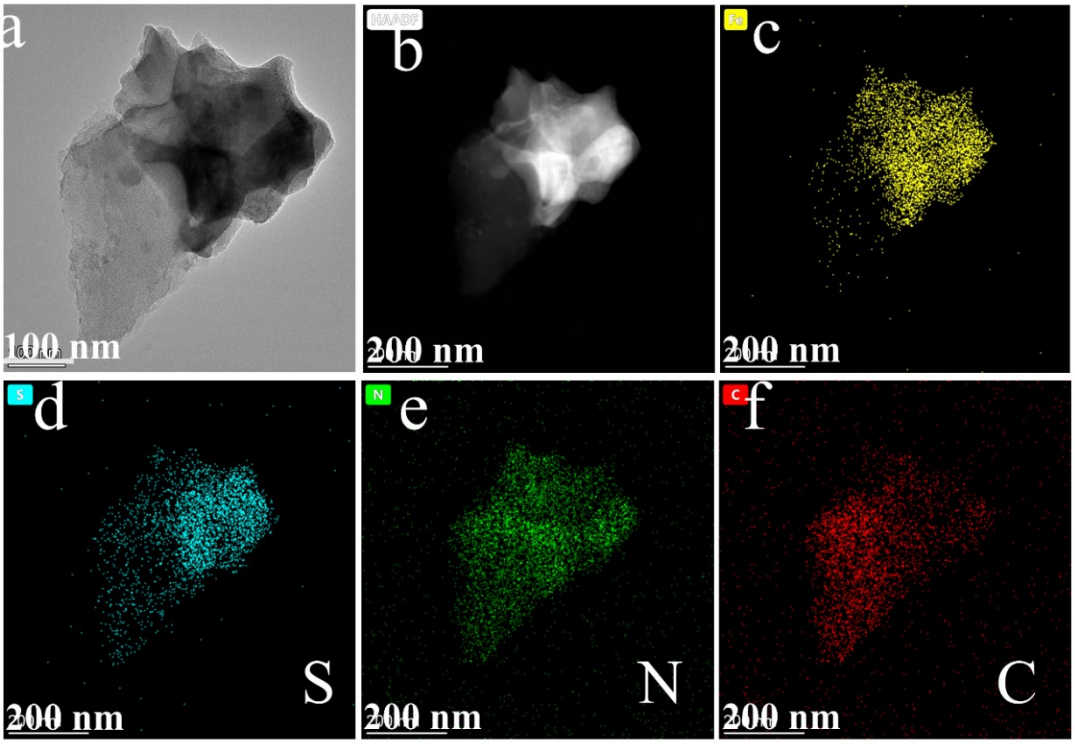

Fig. S5. (a) TEM photo of $Fe_{1-x}S$@NC composite. (b) TEM image and (c-f) the corresponding element distribution maps of $Fe_{1-x}S$@NC composite: Fe, S, N and C.

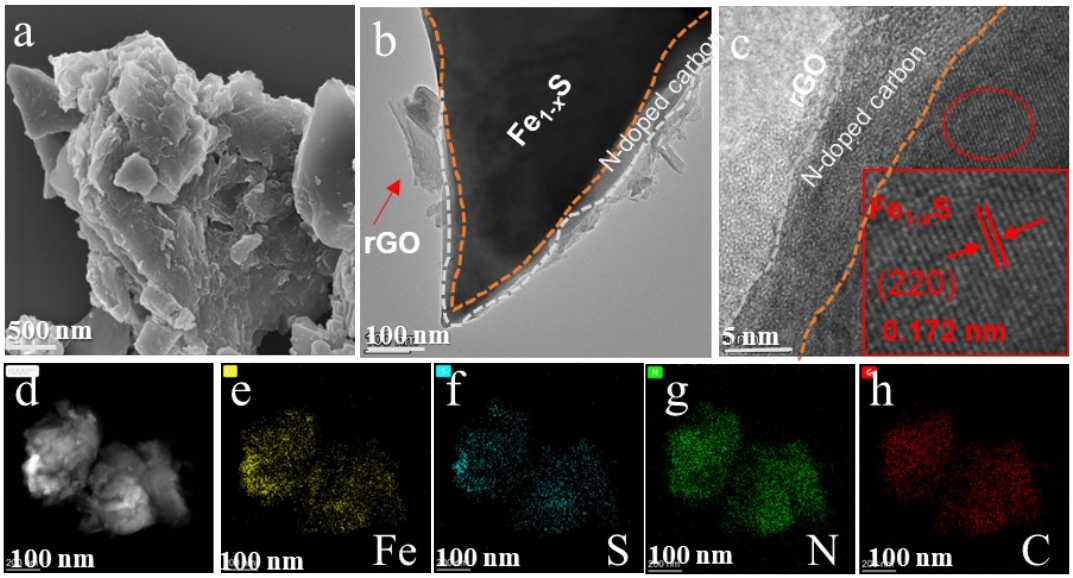

Fig. S6. (a) SEM, (b) TEM and (c) HRTEM images of $Fe_{1-x}S$@NC-rGO-1 composite; (d) TEM image and (e-h) the corresponding element distribution maps of $Fe_{1-x}S$@NC-rGO-1 composites: Fe, S, N and C.

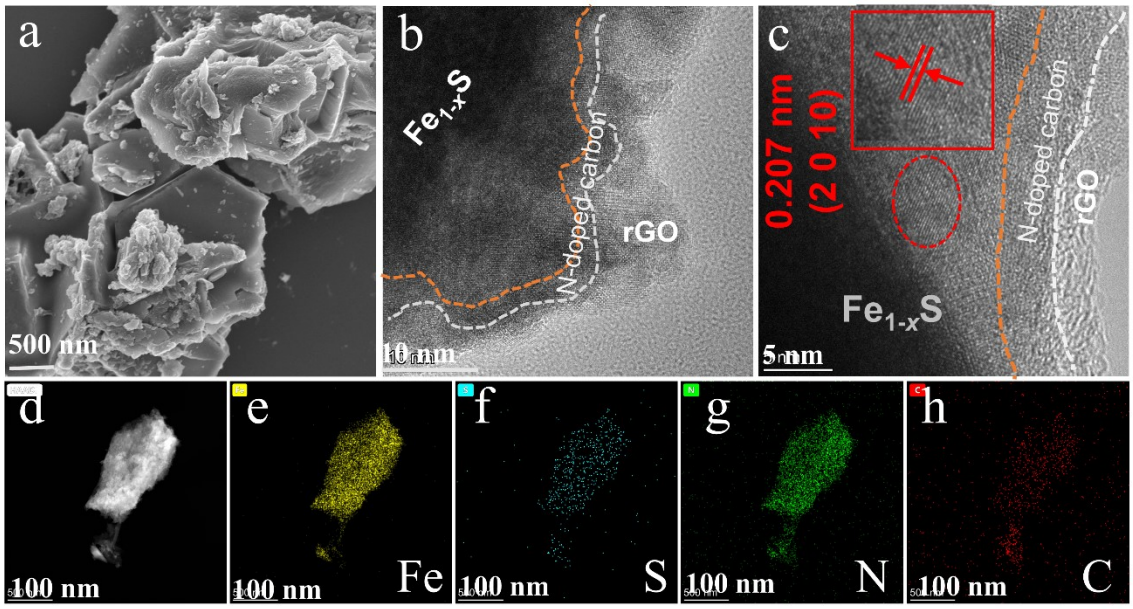

Fig. S7. (a) SEM, (b) TEM and (c) HRTEM images of $Fe_{1-x}S$@NC-rGO-3 composite; (d) TEM image and (e-h) the corresponding element distribution maps of $Fe_{1-x}S$@NC-rGO-3 composites: Fe, S, N and C.

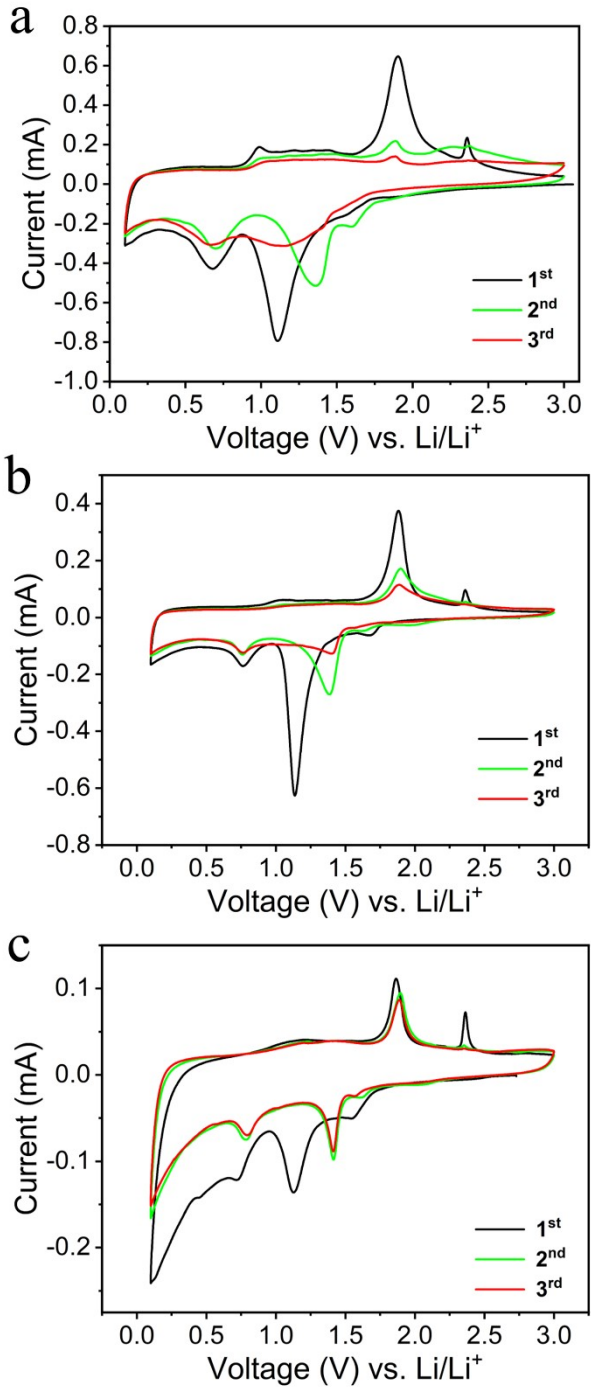

Fig. S8. CV curves of (a) $Fe_{1-x}S$@NC, (b) $Fe_{1-x}S$@NC-rGO-1 and (c) $Fe_{1-x}S$@NC-rGO-3 composites.

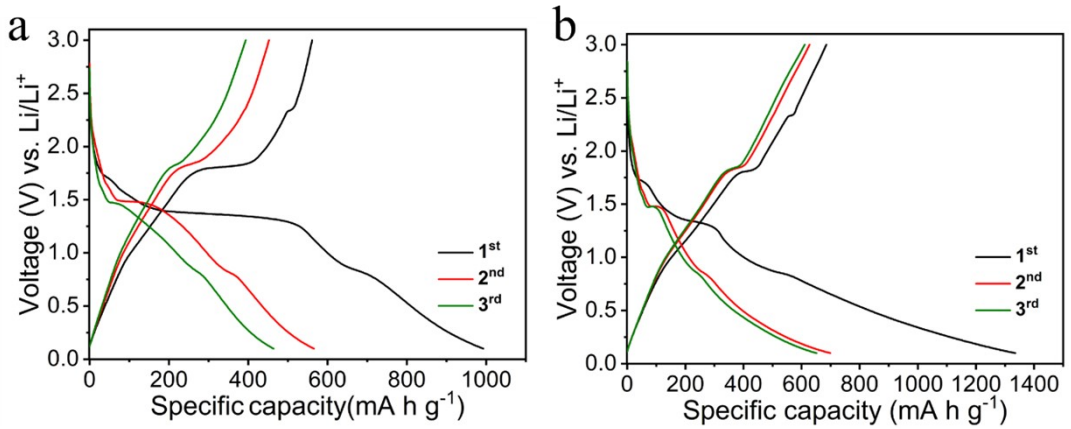

Fig. S9. The capacity voltage diagram of (a) $Fe_{1-x}S$@NC-rGO-1 and (b) $Fe_{1-x}S$@NC-rGO-3 composites.

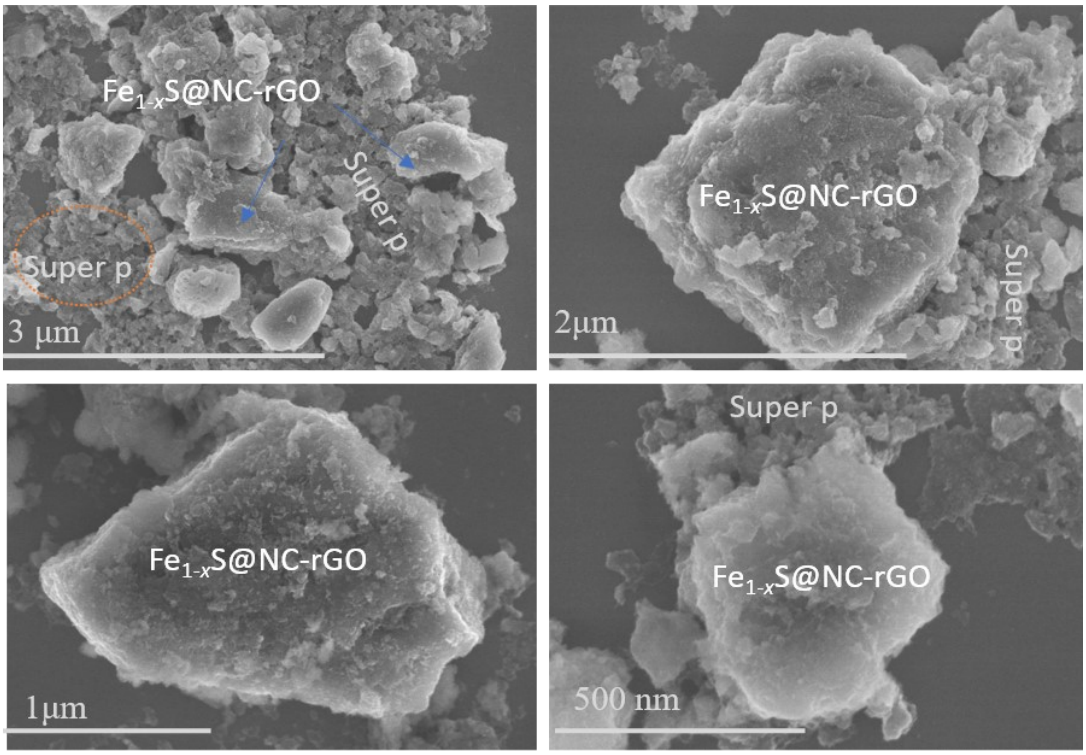

Fig. S10. Different magnifications of SEM images for $Fe_{1-x}S$@NC-rGO-2 electrode after 1700 cycles at 1 A g^{-1}.

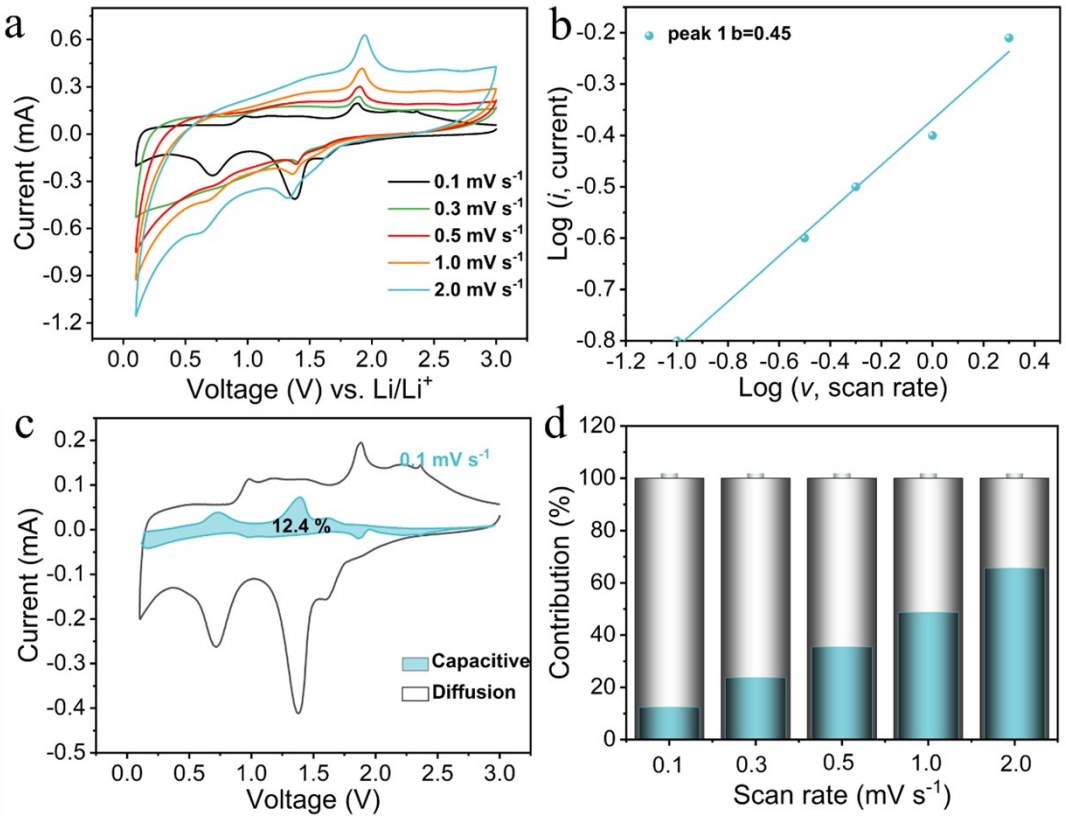

Fig. S11. (a) CV curves of $Fe_{1-x}S$@NC composites at different scan rate range of 0.1 – 2.0 mV s^{-1}. (b) The relationship between log (*i*) and log (*v*). (c) Contribution diagrams of capacitance and diffusion control at the scan rate of 2.0 mV s^{-1}. (d) The contribution ratio of pseudocapacitance behavior of $Fe_{1-x}S$@NC composites at different scan rates.

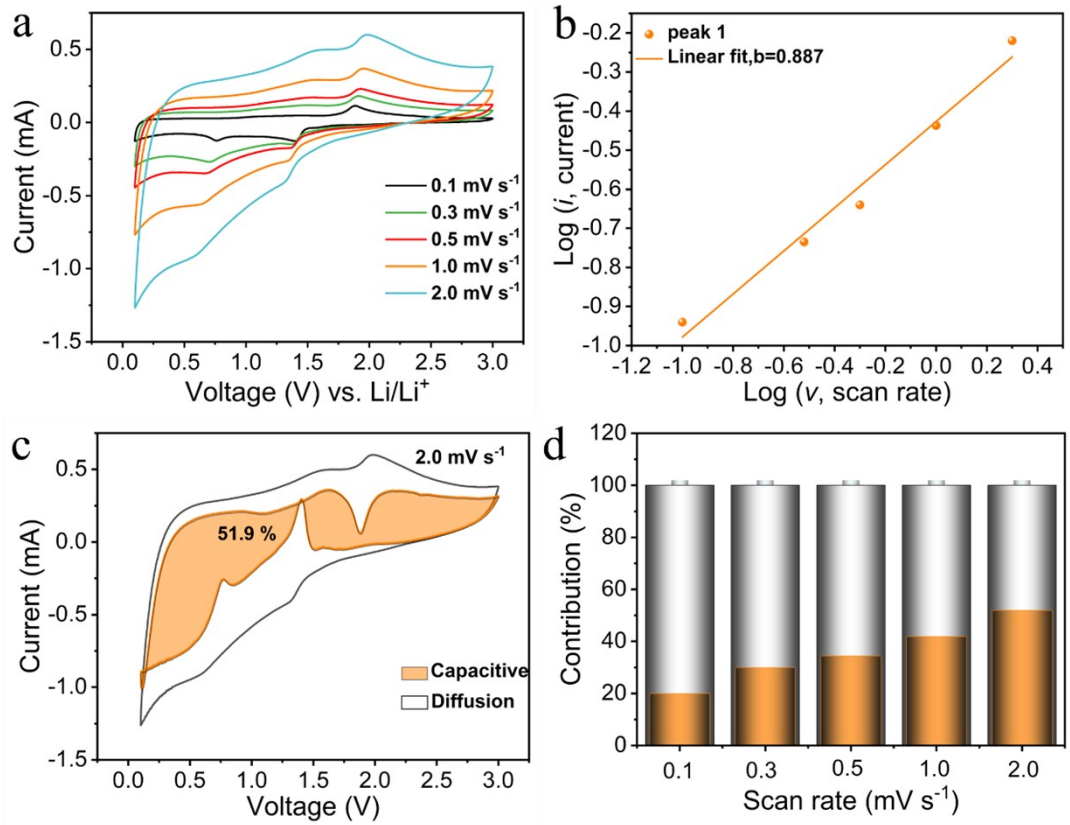

Fig. S12. (a) CV curves of $Fe_{1-x}S$@NC-rGO-1 composites at different scan rate range of 0.1-2.0 mV s^{-1}. (b) The relationship between log (*i*) and log (*v*). (c) Contribution diagrams of capacitance and diffusion control at the scan rate of 2.0 mV s^{-1}. (d) The contribution ratio of pseudocapacitance behavior of $Fe_{1-x}S$@NC-rGO-1 composites at different scan rates.

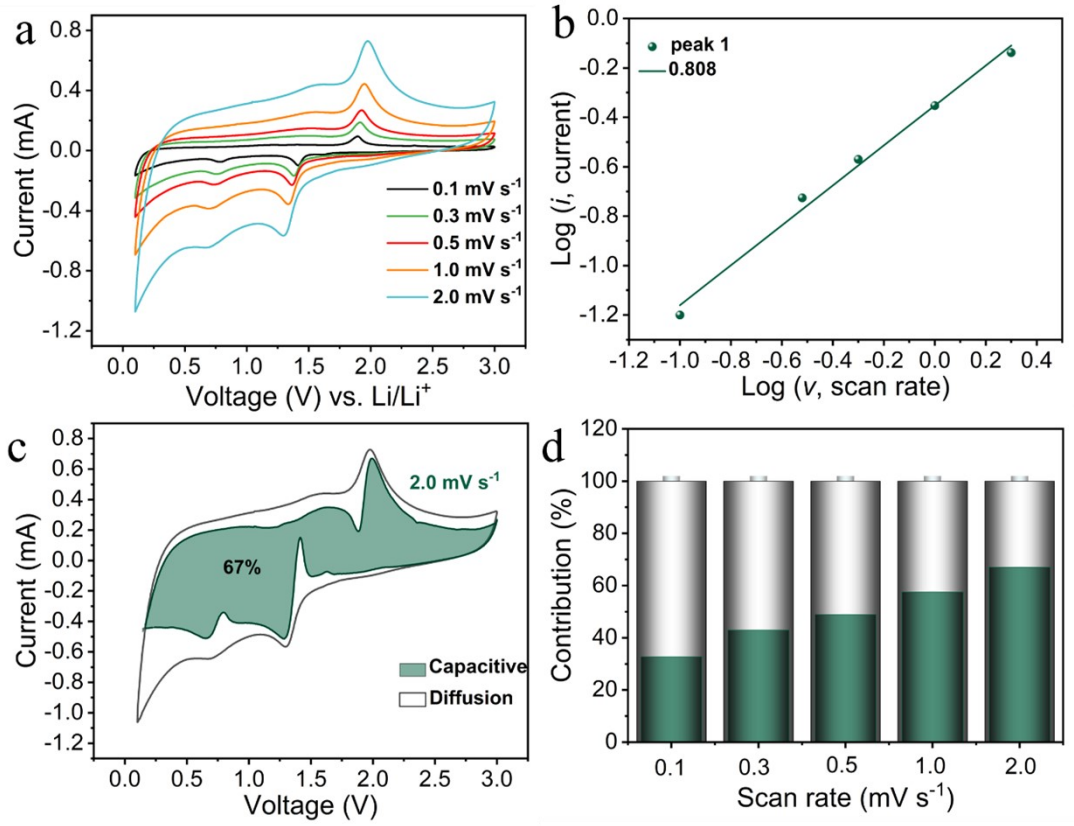

Fig. S13. (a) CV curves of $Fe_{1-x}S$@NC-rGO-3 composites at different scan rate range of 0.1-2.0 mV s^{-1}. (b) The relationship between log (*i*) and log (*v*). (c) Contribution diagrams of capacitance and diffusion control at scan rate of 2.0 mV s^{-1}. (d) The contribution ratio of pseudocapacitance behavior of $Fe_{1-x}S$@NC-rGO-3 composites at different scan rates.

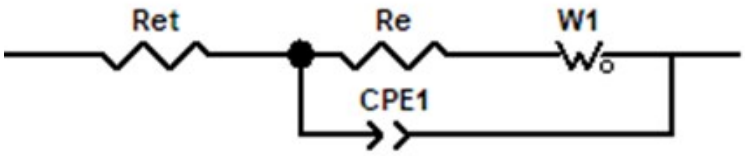

Fig. S14. (a) Equivalent circuit used to fit the Nyquist plots.

References

1 J. Yang, T. Mori and M. Kuwabara, *ISIJ. Int.*, 2007, **47**, 1394-1400.

2 Y. Zhang, H. Xu, P. Li, P. Han, Y. Huang and M. Liu, *Inorg. Chem. Commun.*, 2022, **137**, 109211.

3 Y. Teng, Y. Xu, X. Cheng, S. Gao, X. Zhang, H. Zhao and L. Huo, *J. Alloys. Compd.*, 2022, **909**, 164707.

4 D. Ju, X. Cao, H. Li, J. Zheng, C. Chen, Z. Wang, J. Qiu, Y. Zhang, M. Liu and Q. Zhu, *Ceram. Int.*, 2022, **48**, 13508-13515.

5 Y.-L. Hou, J. Zhang, T. Qin, R. Zeng, H.-B. Guan, S.-G. Wang and D.-L. Zhao, *Appl. Surf. Sci.*, 2022, **599**, 154042.

6 Q. Li, Y. Liu, S. Wei, L. Xu, X. Wu and W. Wu, *J. Electroanal. Chem.*, 2021, **903**, 115848.

7 Z. M. Sheng, N. N. Li, Q. M. Xu, C. Y. Hong, S. Y. Wu, C. K. Chang, S. Han and C. M. Li, *Sustain. Energ. Fuels*, 2021, **5**, 4080-4086.

8 X. Miao, H. Li, L. Wang, Y. Li, D. Sun, X. Zhou and Z. Lei, *J. Mater. Sci.*, 2020, **55**, 12139-12150.

9 J. Xie, J. Carrasco, R. Li, H. Shen, Q. Chen and M. Yang, *J. Power. Sources*, 2019, **431**, 226-231.

10 X. Wei, X. Tan, J. Meng, X. Wang, P. Hu, W. Yang, S. Tan, Q. An and L. Mai, *Nano Res.*, 2018, **11**, 6206-6216.

11 Q. Ma, H. Song, Q. Zhuang, J. Liu, Z. Zhang, C. Mao, H. Peng, G. Li and K. Chen, *Chem. Eng. J.*, 2018, **338**, 726-733.

12 H. Chen, X. Ma and P. K. Shen, *J. Alloys. Compd.*, 2019, **779**, 193-201.

13 M. Huang, A. Xu, H. Duan and S. Wu, *J. Mater. Chem. A*, 2018, **6**, 7155-7161.

14 Y. Du, S. Wu, M. Huang and X. Tian, *Chem. Eng. J.*, 2017, **326**, 257-264.

15 F. Zhang, C. Wang, G. Huang, D. Yin and L. Wang, *J. Power. Sources*, 2016, **328**, 56-64.

16 Y. Xu, W. Li, F. Zhang, X. Zhang, W. Zhang, C.-S. Lee and Y. Tang, *J. Mater. Chem. A*, 2016, **4**, 3697-3703.

17 Z.-G. Wu, J.-T. Li, Y.-J. Zhong, J. Liu, K. Wang, X.-D. Guo, L. Huang, B.-H. Zhong and S.-G. Sun, *J. Alloys. Compd.*, 2016, **688**, 790-797.

18 L. Li, C. Gao, A. Kovalchuk, Z. Peng, G. Ruan, Y. Yang, H. Fei, Q. Zhong, Y. Li and J. M. Tour, *Nano. Res.*, 2016, **9**, 2904-2911.

19 A. K. Haridas, H. Kim, C.-H. Choi, H.-J. Ahn and J.-H. Ahn, *Appl. Surf. Sci.*, 2021, **554**, 149587.

20 J. Zhao, Z. Hu, D. Sun, H. Jia and X. Liu, *Nanomater.*, 2019, **9**, 492.

21 Z. Cao, X. Ma, W. Dong and H. Wang, *J. Alloys. Compd.*, 2019, **786**, 523-529.

22 J. Ma, J. Du, J. Lv, H. Jia, M. Zhang, Y. Nie, B. Ren, B. Hai and S. Zhang, *J. Mater. Sci.: Mater. Electron.*, 2021, **32**, 6788-6798.

23 J. Lv, J. Du, H. Jia, J. Ma, S. Zheng, Y. Nie, K. Song and L. Bai, *Ceram. Int.*, 2020, **46**, 9485-9491.

24 Z. Yan, W. He, X. Zhang, X. Yang, Y. Wang, X. Zhang, Y. Lou and G. Xu, *J. Mater. Sci.: Mater. Electron.*, 2019, **30**, 4527-4540.

25 X. Xu, Q. Ma, Z. Zhang, H. Peng, J. Liu, C. Mao and G. Li, *J. Alloys Compd.*, 2019, **797**, 952-960.

26 M.-H. Wang, H.-G. Xue and S.-P. Guo, *J. Mater. Res.*, 2019, **34**, 3186-3194.